ELSEVIER

Artificial Intelligence in Medicine 29 (2003) 225–239

Artificial Intelligence in Medicine

www.elsevier.com/locate/artmed

The application of fuzzy-based methods to central nerve fiber imaging

Hubertus Axer[a,*], Jan Jantzen[b], Diedrich Graf v. Keyserlingk[a], Georg Berks[a]

[a]*Department of Anatomy I, Universitätsklinikum der RWTH Aachen, Pauwelsstr. 30, D-52057 Aachen, Germany*
[b]*Oersted-DTU, Automation, Technical University of Denmark, DK-2800 Kongens Lyngby, Denmark*

Received 8 August 2000; received in revised form 9 May 2001; accepted 17 June 2001

Abstract

This paper discusses the potential of fuzzy logic methods within medical imaging. Technical advances have produced imaging techniques that can visualize structures and their functions in the living human body. The interpretation of these images plays a prominent role in diagnostic and therapeutic decisions, so physicians must deal with a variety of image processing methods and their applications. This paper describes three different sources of medical imagery that allow the visualization of nerve fibers in the human brain: (1) an algorithm for automatic segmentation of some parts of the thalamus in magnetic resonance images based on the differences in myelin content in various thalamic subnuclei; (2) polarized light for classifying the 3D orientation of the nerve fibers at each point; and (3) confocal laser scanning microscopy (CLSM) for calculating semiquantitative variables for myelin content. Fuzzy logic methods were applied to analyze these pictures from low- to high-level image processing. The solutions presented here are motivated by problems of routine neuroanatomic research demonstrating fuzzy-based methods to be valuable tools in medical image processing.

Keywords: Medical imaging; Fuzzy sets; Classification; Anatomical atlas; White matter; Human brain; Myelin

1. Introduction

1.1. Medical image processing

Technical advances in medicine have led to the development of a wide range of imaging procedures, starting with the discovery of X-rays by Roentgen in 1895 and currently centered on digital image processing.

* Corresponding author. Present address: Department of Neurology, Friedrich-Schiller University Jena, Philosophenweg 3, D-07740 Jena, Germany. Tel.: +49-3641-35005; fax: +49-3641-35399.
E-mail address: hubertus.axer@med.uni-jena.de (H. Axer).

0933-3657/$ – see front matter © 2002 Published by Elsevier B.V.
PII: S0933-3657(02)00071-4

Table 1
Some sources of medical images

Types of images/data sets	Types of information	Imaging procedure
Gray scale images	2D projection of a volume	Radiography Polarized light microscopy Fluorescence microscopy
	Single slices	Computed tomography (CT) Magnetic resonance imaging (MRI) Confocal laser scanning microscopy (CLSM) Transmission electron microscopy (TEM) Ultrasound
	Surfaces	Raster electron microscopy (REM)
Color images	2D projection of a volume	Conventional light microscopy
Colored (functional) data	Diffusion tensor maps	Diffusion weighted-MRI (DW-MRI)
	Blood flow	Functional magnetic resonance imaging (fMRI)
	Blood flow	Positron emission tomography (PET)
	Blood flow, metabolism	Single photon emission computer tomography (SPECT)
Complex data sets	Sequential stacks	z-series: CLSM, CT, MRI Time series: CLSM
	3D data sets and 3D reconstruction	
Multisource information fusion	Atlas–patient matching	

Medical imaging—which primarily focuses on anatomy [8,10]—subsumes the processing and analysis of digital pictures, which show structural or functional aspects of the human body. The interpretation of these images is an important part of diagnostic and therapeutic decisions. Physicians must deal with the acquisition, visualization, processing, and interpretation of digital images. Table 1 gives some examples of different sources of medical images, ranging from grey scale over color images to sequential stacks of images and 3D data sets. Most images contain information about the structure of the human body, but some visualize functional aspects, such as metabolism or blood flow.

The human brain has been imaged frequently, using techniques such as CT, MRI, PET, or SPECT. The brain consists of two main types of tissue, the gray and the white matter. Information is processed in the gray matter, while the purpose of the white matter, which consists of intermingled bundles of fibers, is to carry information from one cerebral region to another over distances ranging from centimeters to meters. The white matter plays a significant role in neurosurgery, because lesions of the white matter can produce severe handicaps.

This paper describes some applications of imaging of the cerebral white matter, demonstrating questions that can be solved by fuzzy image processing. Fuzzy methods are only a part of digital imaging procedures, but the use of linguistic variables [18] as

descriptions of mathematical functions in natural language facilitates the acceptance of fuzzy methods in medicine. Furthermore, many ambiguities in medical image processing can be dealt with by a fuzzy methodology.

1.2. Uncertainties in image processing

Image processing involves acquiring and interpreting these images, as well as comparing them with each other. Different hierarchical levels of image processing can be distinguished [6,16], although they may overlap.

1. Low-level image processing describes the processing of gray values of single pixels, including optimal settings of image acquisition parameters and improvement of contrast or brightness by filtering. Overall, low-level image processing provides images of adequate quality.
2. Intermediate-level image processing detects objects in the image through feature extraction, segmentation, and skeletonization.
3. High-level image processing, which interprets data contained in the image, deals with problems of classification, model matching, and linguistic description. In medicine, the result of such interpretation is generally an image diagnosis.

The methods used in the following examples are quite distinct and application specific, but they represent problems in central nervous fibers research that may be solved by fuzzy methods.

2. Three examples of imaging of central nervous fibers using fuzzy-based methods

Our research focuses on white matter in the human brain [1–5], which consists largely of nerve fibers covered by myelin sheaths. The complex connective architecture of neuronal cells is important to the function of the central nervous system [11]. Different imaging routines are used to visualize the white matter of the brain and the myelin sheaths of the nerve fibers.

2.1. Example 1: myelin content in magnetic resonance images

2.1.1. Problem

In T1-weighted magnetic resonance imaging (MRI) slices, myelin, the fatty component of the central nervous system, is visualized as bright white. This technique can be used to distinguish parts of the thalamus [7], which can be subdivided into myelin-rich and myelin-poor parts. The purpose of this procedure is to automatically segment parts of the thalamus in the 3D neighborhood of each voxel.

2.1.2. Material and methods

A voxel x_i in the MRI data set is characterized by its gray value $g(x_i)$ in $\{0, 1, \ldots, 255\}$. The voxels x_j $(j = 1, \ldots, 26)$ in its 3D $(3 \times 3 \times 3)$ neighborhood also provide some information, which may define the central voxel x_c as an object, an edge, or as noise.

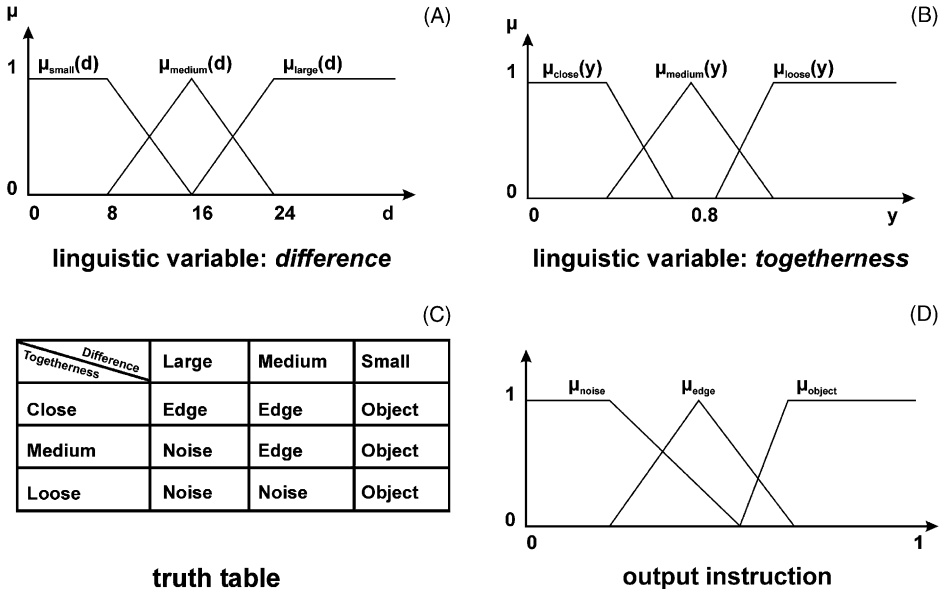

Fig. 1. Membership functions. (A) The membership functions for the linguistic variable *difference*. (B) The membership functions for the linguistic variable *togetherness*. (C) Truth table. (D) The membership functions for the output instruction.

Thus, the gray value of the central voxel x_c is compared with the gray values of the voxels x_j in the direct neighborhood of x_c. The accumulated difference between the central voxel and all 26 touching, neighboring voxels can be computed as

$$\mathrm{d}(x_c, x_j) = \sum_{j=1}^{26} |g(x_c) - g(x_j)|$$

This relationship defines the linguistic variable *difference* as being small, medium, or large using the membership functions shown in Fig. 1A. The membership functions were defined in this way after analysis of the grey scale values of different data sets and the functions were adjusted by trial-and-error. The horizontal axis is the *universe of discourse*, defined as all the possible values of $\mathrm{d}(x_c, x_j)$ that can come into consideration. The vertical axis is the *degree of membership* $\mu(d)$. For instance, a value $\mathrm{d}(x_c, x_j) = 10$ is *small* to the degree 0.75 and *medium* to the degree 0.25.

In addition, the immediate neighbors of the central voxel relate to each other independently of the central voxel. This relationship we call the *togetherness* of the voxel. The input y of the linguistic variable *togetherness* is computed using the function $\mathrm{d}(x_i, x_a)$ that examines whether there is a coherent region a_{coh} of voxels with similar gray values:

$$a_{\mathrm{coh}} = \{x_a || g(x_i) - g(x_a)| \leq \beta\}, \qquad \mathrm{d}(x_i, x_a) = \sum_{a=1}^{n} |g(x_i) - g(x_a)|$$

where the set a_{coh} is the set of voxels in the 3D neighborhood belonging to a unity of gray values that have similar values. The value $\mathrm{d}(x_i, x_a)$ is the accumulated difference between a voxel x_i in a_{coh} and all n voxels in a_{coh} (including itself, but the difference is zero and does not contribute). Only if the difference between x_i and x_a is smaller than a threshold β, the point x_a is counted as a member of a_{coh}. The value of β was set to 8 in this case because trial-and-error showed that it provided the best results. The togetherness is defined by means of a function $y(x_i)$:

$$y(x_i) = \frac{m \times 255 + \mathrm{d}(x_i, x_a)}{y_{\max}}$$

where y is a number in the interval [0, 1] and m is the number of pixels outside of the region a_{coh} ($m = 26 - n$). For normalization, the numerator is divided by the maximum amount $y_{\max} = 26 \times 255$. Consequently, for $m = 26$, $y(x_i) = 1$, and for $m = 0$, y approaches zero when d approaches zero. The *togetherness* (Fig. 1B) can be described as *close* if the value y is rather small and as *loose* if y is large.

The resulting procedure on the central voxel depends on both *difference* and *togetherness*. A pre-run checks whether all surrounding voxels have large differences (large d) and close togetherness (large m). In this case, the central voxel is regarded as noise and is replaced by the voxel with the smallest difference. Otherwise the variables *difference* and *togetherness* are used to derive rules (Fig. 1C), for example:

If difference is small and togetherness is close, then the voxel is treated as object.

The resulting instructions are computed according to the Mamdani controller [9] and the mean of maxima defuzzification [19]. The membership functions of the input values d and y determine the antecedent of the different rules. The degree of match α_r of the rule r is achieved by the min-operator (aggregation).

$$\alpha_r = \min\{\mu_{r,p}(d), \mu_{r,q}(y)\}, \quad p \in \{\text{small}, \text{medium}, \text{large}\},$$
$$q \in \{\text{close}, \text{medium}, \text{loose}\}, \quad r \in \{1, 2, \ldots, R\}$$

The membership functions (Fig. 1D) for the output values are then

$$\mu_r^{\text{cons}}(x_i) = \min\{\alpha_r, \mu_r^k\}, \quad k \in \{\text{noise}, \text{edge}, \text{object}\}$$

where μ_r^k is the membership function of the consequent of rule r, and k is one of the terms: *noise*, *edge*, or *object* (implication).

From aggregation and implication of the membership functions of the rules, the resulting membership function of all R rules together is selected by the max-operator (accumulation)

$$\mu_{\text{res}}(u) = \max_r\left\{\mu_r^{\text{cons}}(x_i)\right\}, \quad r = 1, 2, \ldots, R$$

Defuzzification is performed by calculating the value g_{weight} by the mean of maximum. This value gives the weighting factor for the central voxel x_c when its gray value, $g_{\text{res}}(x_c)$, is calculated:

$$g_{\text{res}}(x_c) = \frac{\sum_{i=1}^{27} g(x_c) g_{\text{weight}} + g(x_i)}{27}$$

(27 is the number of voxels in the analyzed volume—1 central voxel and 26 neighboring voxels).

2.1.3. Results

After applying the fuzzy segmentation method, small contiguous regions with voxels of similar gray value appear, which correspond quite well to the histologically known nuclei of the thalamus (Fig. 2). This congruence becomes apparent when a digital 3D atlas [15] is superimposed on the segmented images. Fig. 2A shows a section through the segmented myelin-rich voxels. In the pons these voxels represent the pontocerebellar fibers and fibers of the pyramidal tract. The segmented voxels in the thalamus (outlined in dark grey) mainly represent the ventral nuclei of the thalamus. Fig. 2B shows the atlas projected onto the non-segmented MRI slice.

Fig. 2C shows a section through the segmented myelin-poor voxels and Fig. 2D shows the outline of the thalamus as presented in the atlas. The myelin-poor voxels correspond well to the nucleus dorsomedialis of the thalamus (Fig. 2E), while the myelin-rich nuclei

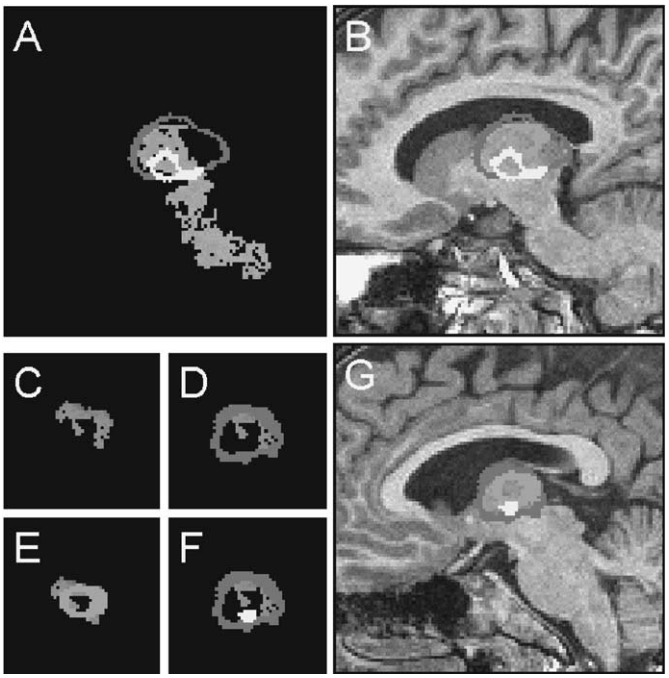

Fig. 2. Match of voxels isolated by means of fuzzy set application and substructures of the thalamus according to the atlas. (A) Group of isolated myelin-rich voxels. The outline of the thalamus as represented in the atlas is shown in dark grey. The nuclei ventrales are shown in bright grey. (B) The atlas as in A projected onto the non-segmented MRI data set. (C) Group of isolated myelin-poor voxels. (D) Correspondence of parts of the isolated voxels to the nucleus dorsomedialis of the thalamus. (E) Outline of the thalamus surrounding the myelin-poor voxels. (F) The myelin-rich nuclei ventrales (in bright grey) are positioned in the spared area of the segmented voxels. (G) The atlas as in (D)–(F) projected onto the non-segmented MRI data set.

ventrales are located in the spared area (Fig. 2F). Fig. 2G shows the atlas projected onto the non-segmented MRI data set.

2.1.4. Discussion of the example

Areas in the thalamus, which cannot be seen in the original MRI data set, were segmented automatically. Some subnuclei of the thalamus are targets of functional neurosurgery (e.g. the nucleus ventrointermedius in pharmacoresistant tremor). An atlas can be projected onto the patient's brain to calculate the 3D locations of these subnuclei. An automatic segmentation of myelin-rich and myelin-poor parts of the thalamus can be used to evaluate the correctness of the fit of the atlas to the individual brain.

Procedures for segmentation using crisp thresholds did not lead to acceptable results. Fuzzy methods were applied in this case because rules could be described using natural language. The solution had two effects: the algorithm detects noise and suppresses it, and a 3D segmentation is performed simultaneously. The idea of using the myelin content in the different thalamic nuclei to map this area came from expert anatomical knowledge. The tool for expressing this knowledge was the fuzzy rule base.

2.2. Example 2: 3D orientation of central nervous fibers using polarized light

2.2.1. Problem

Researchers have studied the architecture of the cerebral white matter in the human brain since the beginning of the last century [13]. The 3D orientation of nerve fibers in the brain can help define these fibers as parts of distinct functional systems [3,4]. The course and location of fiber tracts in the brain is very important in neurosurgical procedures because damage to these tracts can cause severe handicaps in the patient.

To generate maps of the 3D orientation of nerve fibers automatically, the physical principle of polarized light microscopy was applied. In plane-polarized light, the electromagnetic waves of the light are oriented in a single plane. Light becomes plane-polarized by passing through a polarization filter (polarizer) before it passes through the sample. Anisotropic structures in the sample, which show different measurements when measured in different directions, bend the light so that it can pass through a second polarizing filter (analyzer) perpendicular to the first polarization filter and can be imaged. The amount of light bent depends on the amount and spatial orientation of the anisotropic tissue. Radially oriented lipids in the myelin sheaths of the nerve fibers cause *birefringence*, a refraction of light to form two rays from one. Thus, order and orientation of the fibers determine the polarization picture of the section under different rotation angles of the polars (azimuth).

2.2.2. Material and methods

Unstained sections of formalin-fixed and polyethylene glycol (PEG)-embedded human brains were used for this purpose. The slices, 100 μm thick, were placed in a fixed position between two rotatable, crossed polarizing filters and illuminated. A digital camera took nine pictures of the section under azimuths from 0 to 80°, and a set of nine grey scale values of light intensity (g_0 to g_{80}) was assigned to each point in the section:

$$A_{xy} = \{g_0(xy), g_{10}(xy), \ldots, g_{80}(xy)\}$$

The grey scale values were normalized by dividing by 255, chosen because it is simple. The settings of the imaging system, such as brightness and contrast, were adjusted at first so that the histograms of the pictures spanned the entire interval of grey scale values ranging from 0 to 255 as in the function $f_{\text{angle}}(xy)$:

$$f_{\text{angle}}(xy) = \frac{g_{\text{angle}}(xy)}{255}$$

$$\tilde{A}_{xy} = \{f_0(xy), f_{10}(xy), \ldots, f_{80}(xy)\}$$

The nine intensity values contain information about the 3D orientation of the nerve fibers at this point. The *inclination* of the fibers is defined as the elevation of the fibers in the z-direction of the section, while the *direction* describes the orientation of the fibers in the xy-plane of the section.

Fuzzy logic methods were applied to classify the inclination of fibers [2]. Two interesting parameters (Fig. 3A) were defined in the sequence of measurements, which give information about the inclination of the fibers at each point. The brightest intensity in the sequence is one parameter. The flatter the fibers' orientation, the brighter the pixels are under a certain azimuth or, conversely, as fibers get steeper the brightest pixel becomes less bright.

In contrast, the flatter the fibers run, the more accentuated the peak will be, so the second parameter is defined as the width of the peak. A threshold value (0.6), determined by testing different values, was defined to eliminate low intensities. Both *intensity* and *peak-width* were described by fuzzy variables. *Peak-width* was defined as none, narrow, and broad

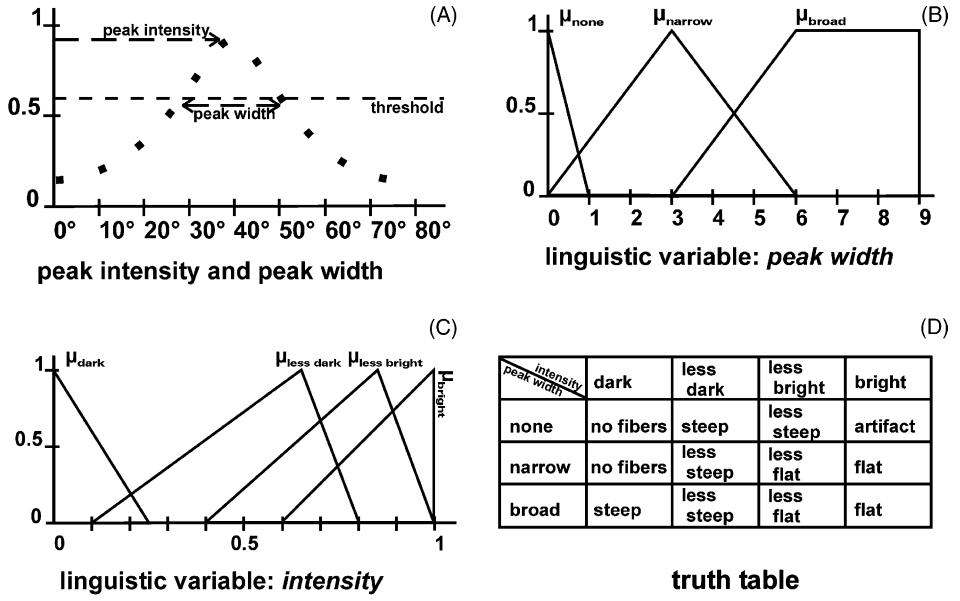

intensity / peak width	dark	less dark	less bright	bright
none	no fibers	steep	less steep	artifact
narrow	no fibers	less steep	less flat	flat
broad	steep	less steep	less flat	flat

Fig. 3. Intensity values and linguistic variables. (A) Intensity values under rotation of the polars (x-axis). (B) Linguistic variable *peak-width*. (C) Linguistic variable *intensity*. (D) Truth table.

using the functions in Fig. 3B. The four descriptions of *intensity* were defined as dark, less dark, less bright, and bright, and were calculated according to the graphs in Fig. 3C.

The classes of fiber inclination are steep, less steep, less flat, and flat. The method also detects pixels containing no fibers, e.g. in the gray substance or the ventricular system. The relations are defined in the truth table shown in Fig. 3D. The truth table describes rules such as

> If the highest intensity is bright and the peak-width is narrow, then the course of fibers will be flat.

Such rules can be mathematically processed as the minimum value of the membership functions of intensity (bright) and peak-width (narrow).

$$\mu_{\text{flat}} = \min(\mu_{\text{bright}}, \mu_{\text{narrow}})$$

Defuzzification is done by searching the rule with the highest membership function and classifying each pixel according to the fiber inclination at the respective point. The classes of fiber inclination are visualized as different grey scale values.

This method also allows definition of areas of the cerebral gray matter. This classification can be done very easily, because all nine intensities have to be dark. Thus, the membership function of a pixel belonging to the gray matter can be defined as

$$\mu_{\text{grey-matter}} = \min(\mu_{\text{dark}}(0^\circ), \mu_{\text{dark}}(10^\circ), \ldots, \mu_{\text{dark}}(80^\circ))$$

In addition, the direction of the nerve fibers is represented by that azimuth where the lowest intensity of light can be measured (when using a quarter-wave plate as additional filter). Thus, both inclination and direction can be assessed automatically in each point of the section.

2.2.3. Results

Fig. 4A shows a fiber inclination map. The four classes of inclination are visualized as increasing grey scale values. Black indicates that no fibers are located at this point (gray matter, no brain tissue, artifacts). A fiber direction map of the same section can be seen in Fig. 4B. Here, the angles of direction (0–180°) are shown as increasing grey scale values; 0° means that the fibers are oriented parallel to the *x*-axis of the picture.

Inclination and direction are also shown in arbitrarily selected points in the section using lines (Fig. 4C). The direction of each line shows the direction of the fibers, and the class of inclination determines the length of the line. Different grey scales represent different tracts of fibers.

2.2.4. Discussion of the example

The two parameters, namely the height and the width of the intensity peak, seem to be related: the broader the peak, the lower the height. This is the case for pixels that represent fibers, but many pixels represent other tissues such as gray matter, ventricle, and artifacts caused by crystals from the histological preparation. Thus, height and width of the intensity peak are well suited to detect artifacts in the images because here height and width are not related. Moreover, the use of both parameters makes the algorithm very robust. The polarization effects of the tissue are dependent on parameters such as thickness of the

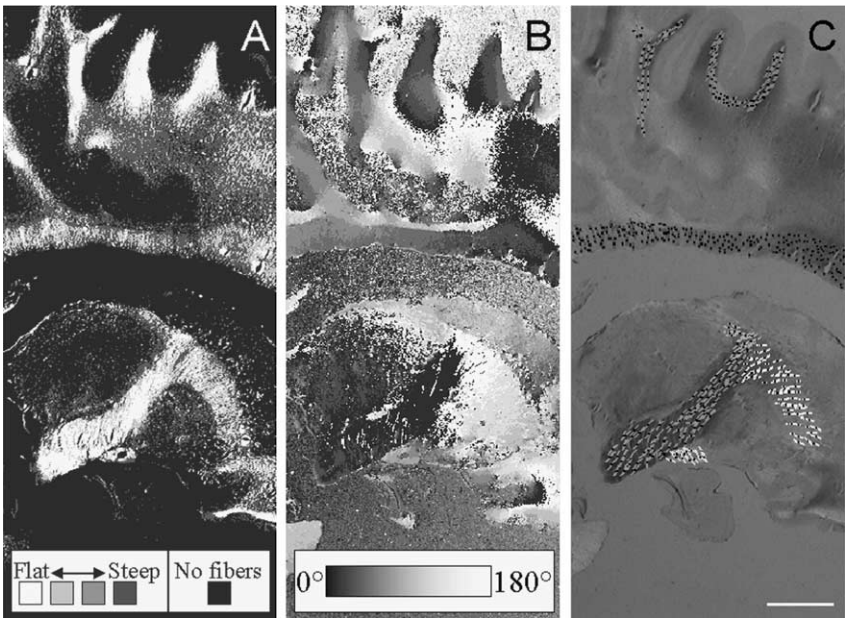

Fig. 4. A sagittal section through the human brain. (A) Inclination of the fibers is visualized as different grey scale values. (B) Direction of the fibers is shown as different grey scale values (0° means the fibers are oriented parallel to the *x*-axis of the picture). (C) Different selected fiber tracts are shown as lines. Different grey scale values represent different systems of fibers. The direction of the line shows the direction of fibers while the length of the line shows the inclination of fibers. Scalebar: 10 mm.

slices, magnification, and contrast. The use of this rule-based system allows the visualization of fiber orientation in variable settings of the imaging system and thus is a tool for fast visualization of the fiber structure [2]. This fuzzy system is useful for both a rough classification of fiber inclination and the classification of gray matter and artifacts.

2.3. Example 3: myelin content in confocal laser scanning microscopic images

2.3.1. Problem

Confocal laser scanning microscopy (CLSM) produces optical sections through a fluorescent sample. In CLSM, sequential scanning by a laser measures the fluorescence in these voxels [17]. So-called *z*-series of optical sections, a sequence of specimen sections along the *z*-axis perpendicular to the *xy*-plane, can be used to perform 3D reconstruction of the nerve fibers [3].

Nerve fibers can be labeled with fluorescent, lipophilic carbocyanine dyes (e.g. 1,1′-dilinoleyl-3,3,3′,3′-tetramethylindocarbocyanine perchlorate (DiI)), which diffuse into all lipophilic structures in the sample, e.g. the myelin sheaths. These confocal images represent measurements of the fluorescent dye in each pixel, so the architecture of the myelinated fibers in the brain can be imaged exactly (Fig. 5).

Another physical method, electrical impedance, can show the architecture of myelinated fibers at the tip of an electrode. In functional neurosurgery, impedance measurements can

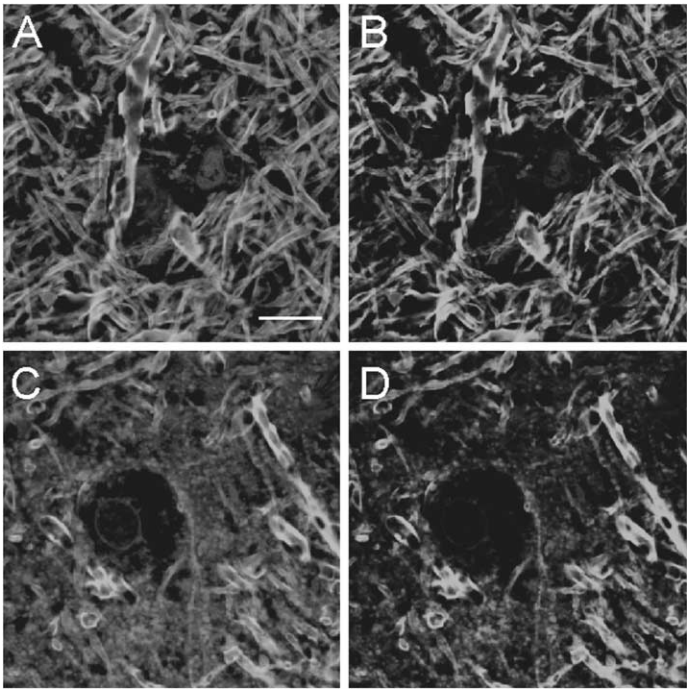

Fig. 5. (A) Cerebral white matter, original picture. (B) Fig. 1A after filtering: the cell nucleus has been diminished, and the nerve fibers have been accentuated. (C) Cerebral gray matter. (D) Fig. 1C after filtering.

be used to evaluate intraoperatively if the stereotactic needle is positioned correctly in the brain [5]. The following procedure was used to demonstrate the correlation between tissue impedance and the myelin content in the brain.

2.3.2. Material and methods

Impedance was measured at 12 characteristic points in a formalin-fixed human brain (Fig. 6A) over a wide range of frequencies (10^2 to 10^6 Hz). These points were then inoculated with the fluorescent marker DiI (*FAST* DiI© oil, Molecular Probes Europe BV, Leiden, The Netherlands), so that the architecture of fibers could be visualized by CLSM (Leica TCS NT, Leica Microsystems, Heidelberg, Germany).

The confocal images were normalized (by dividing the grey scale values $g(x)$ by 255):

$$f(x) = \frac{g(x)}{255}$$

Each value $f(x)$ represents the intensity of fluorescence at point x. The calibration of the imaging system was maintained to ensure a constant relationship between the measurements in the pixels and the intensity of fluorescence in the probes. Other procedures of normalization, such as $z^* = (z - z_{\min})/(z_{\max} - z_{\min})$ (with z as the current pixel value, $z_{\min}$ as the minimum, and $z_{\max}$ as the maximum gray levels of the image), or the use of Zadeh's

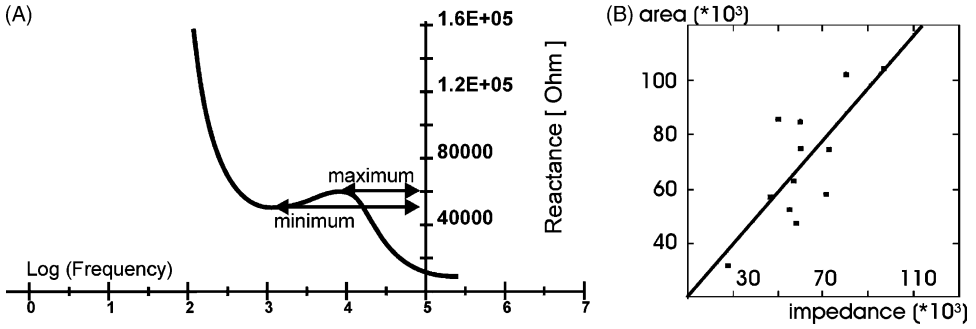

Fig. 6. (A) Impedance measurement in the central nerve tissue performed from 10^2 to 10^6 Hz (x-axis). The reactant part of impedance (in Ω) at the local maximum was chosen as characteristic parameter. (B) Correlation between variable $\text{area}_z(\mu)$, which resembles the myelin content, and the maximum value of the impedance graph.

standard S-function [16] would disturb the linear relationship between gray value and amount of fluorescence.

The values of $f(x)$ were used to estimate the myelin content in the tissue. The highest intensity of fluorescence is caused by the myelin sheaths, but a certain amount of low-intensity fluorescence is caused by other lipophilic cell organelles such as the membrane of the cell nucleus. Consequently, the original confocal images have to be modified and the following intensity-modifier (*contrast intensification*, see, e.g. [16,19]) was used:

$$\mu(x) = \begin{cases} 2[f(x)]^2, & \text{if } 0 \le f(x) \le 0.5 \\ 1 - 2[1 - f(x)]^2, & \text{else} \end{cases}$$

This intensity-modifier was chosen, because it allows low-intensity fluorescence to decrease, while high-intensity fluorescence specific for myelin is increased (Fig. 5), by substituting $\mu(x)$ for $f(x)$, which better describes the content of myelin than $f(x)$ does.

To arrive at a semiquantitative variable representing the content of myelin in the sample, the variable $\text{area}_z(\mu)$ was calculated as a summation of all grades of membership [12]:

$$\text{area}_z(\mu) = \sum_{i=1}^{65\,536} \mu(x_i)$$

Thus, for each point z of impedance measurement, $\text{area}_z(\mu)$ represents the content of myelin at point z. The domain of pixels over which $\text{area}_z(\mu)$ is calculated has to be kept the same shape for comparability. In this example it was defined as a matrix of 256×256 (65 536) pixels. All areas $\text{area}_z(\mu)$ from all samples were correlated to measurements of electrical impedance, and the local maximum of the graph of impedance measurements was chosen as a characteristic parameter, a *feature* (Fig. 6A).

2.3.3. Results

The Pearson correlation coefficient between the value of the reactant part of impedance measured at the local maximum of the impedance graph (Fig. 6A) and variable $\text{area}_z(\mu)$ was 0.737 ($P = 0.01$, Fig. 6B). The number of impedance measurements analyzed here was 12. This result shows that impedance depends on the myelin content, but impedance

values are also dependent on other parameters such as the orientation of the fibers in relation to the electrode [5].

2.3.4. Discussion of the example

The relationship between myelinization and electrical impedance is not new. Electrical impedance also depends on density of fibers, cells, electrolyte concentration, and the orientation of the fibers in relation to the electrode [5]. Thus, a semiquantitative variable of myelin content represents only one parameter influencing impedance measurement. Impedance also depends on the frequency of the injected sinusoidal signal; its relationship to amplitude remains to be investigated. Nevertheless, in neurosurgical environments only measurements at 50 000 Hz are commonly used for defining the borders of different tissues in the brain. However, at this reference frequency, the impedance measurements do not represent the properties of the tissue (for example, the content of myelin) as well as the reference demonstrated here does [5]. This can be demonstrated by comparing histological tissue properties with impedance measurements at different frequencies [5]. The example presented here demonstrates low-level image processing and the use of a fuzzy method is a legitimate solution of the problem.

3. Discussion and conclusion

The three examples presented, all use different imaging methods: CLSM, MRI, and polarized light microscopy. All methods investigated the same object, the cerebral white matter. Processing of these digital images led to new insights into this field of brain research.

Fuzzy methods were applied from low- to high-level image processing. These methods represent only a small range of fuzzy methods. A wider selection of fuzzy techniques can be used in image processing [14,16,19], including fuzzy clustering and fuzzy integrals.

The third example demonstrates an application of low-level image processing. A fuzzy filter was used because the border between high-intensity fluorescence and low-intensity fluorescence cannot be defined as crisp. This uncertainty was handled by fuzzy methods.

The other examples represent intermediate- to high-level image processing. Here, fuzzy logic was used to classify voxels in a 3D MRI data set or pixels in sequences of polarized light images. The advantage of linguistic variables is their potential for generating rules in natural language without using mathematical functions, especially in cases where the exact mathematical function is not known.

The classification of pixels according to the inclination of fibers using fuzzy logic turned out to be very robust. Of course, a crisp mathematical model can be described for the birefringent features of nerve tissue. However, the polarized light images depend heavily on contrast, brightness, magnification, and thickness of the sample. These settings must be kept constant in order to use the crisp mathematical model reliably. In contrast, the fuzzy model can be used to image different magnifications of the sections.

The three examples are quite distinct and application specific, and they represent procedures motivated by problems of routine neuroanatomic research. Thus, it would be very helpful for medical environments to have more general software tools that support the

application of fuzzy methods to medical image processing. Physicians who are not familiar with mathematical formulas would find it helpful to use natural language in the description of biological objects [1].

There are several advantages to using fuzzy methods for medical image processing. Digital images represent data sets that are not fundamentally different from other databases. Relationships and patterns in these data sets must be extracted in order to make a diagnosis. However, a high level of medical expertise is necessary to interpret medical images. Gray scale medical images are fuzzy because they are defined on an interval that can be scaled to [0, 1], and borders between objects are often fuzzy. These uncertainties, including noise, can be processed with fuzzy methods, but it must be understood that the digital images themselves are fuzzy.

Acknowledgements

Some of this work was supported by ERUDIT (http://www.erudit.de), a European network in uncertainty techniques developments for use in information technology, supported by the European Commission.

References

[1] Axer H, Südfeld D, Keyserlingk DGv, Berks G. Fuzzy sets in human anatomy. Artif Intell Med 2001;21:147–52.
[2] Axer H, Berks G, Keyserlingk DGv. Visualization of nerve fiber orientation in gross histological sections of the human brain. Microsc Res Tech 2000;51:481–92.
[3] Axer H, Keyserlingk DGv. Mapping of fiber orientation in human internal capsule by means of polarized light and confocal scanning laser microscopy. J Neurosci Methods 2000;94:165–75.
[4] Axer H, Lippitz BE, Keyserlingk DGv. Morphological asymmetry in anterior limb of human internal capsule revealed by confocal laser and polarized light microscopy. Psychiatry Res Neuroimaging 1999;91:141–54.
[5] Axer H, Stegelmeyer J, Keyserlingk DGv. Comparison of tissue impedance measurements with nerve fiber architecture in human telencephalon: value in identification of intact subcortical structures. J Neurosurg 1999;90:902–9.
[6] Berks G, Keyserlingk DGv. Fuzzy sets in medical image processing. In: Szczepaniak PS, Lisboa PJG, Kacprzyk J, editors. Fuzzy systems in medicine. Heidelberg: Physical-Verlag; 2000. p. 281–315.
[7] Berks G, Keyserlingk DGv. Automatic support of medical image processing with fuzzy application. In: Jamshidi M, Bien Z, Fathi, M, editors. Soft computing, multimedia and image processing, vol. 8. Albuquerque: TSI press; 1998. p. 583–90.
[8] Brinkley JF, Rosse C. The digital anatomist distributed framework and its applications to knowledge-based medical imaging. JAMIA 1997;4:165–83.
[9] Mamdani EH. Application of fuzzy logic to approximate reasoning. IEEE Trans Comput 1977;26: 1182–91.
[10] Margulis AR, Sunshine JH. Radiology at the turn of the millennium. Radiology 2000;214:15–23.
[11] Mesulam MM. Large-scale neurocognitive networks and distributed processing for attention, language, and memory. Ann Neurol 1990;28:597–613.
[12] Pal SK, Gosh A. Fuzzy geometry in image analysis. Fuzzy Sets Syst 1992;48:23–40.
[13] Rye DB. Tracking neural pathways with MRI. TINS 1999;22:373–4.
[14] Sadegh-Zadeh K. Advances in fuzzy theory. Artif Intell Med 1999;15:309–23.

[15] Schaltenbrand G, Wahren W. Atlas for stereotaxy of the human brain. 2nd ed. Stuttgart: Thieme; 1977.
[16] Tizhoosh HR. Fuzzy Bildverarbeitung. 1st ed. Berlin: Springer; 1998.
[17] Wright SJ, Centonze VE, Stricker SA, DeVries PJ, Paddock SW, Schatten G. Introduction to confocal microscopy and three-dimensional reconstruction. Methods Cell Biol 1993;38:1–45.
[18] Zadeh LA. The concept of a linguistic variable and its applications to approximate reasoning-I. Inform Sci 1975;8:199–249.
[19] Zimmermann HJ. Fuzzy set theory. 3rd ed. Boston: Kluwer Academic Publishers; 1996.